Chemical Science

ROYAL SOCIETY OF CHEMISTRY

EDGE ARTICLE

View Article Online
View Journal | View Issue

Cite this: *Chem. Sci.*, 2022, **13**, 10082

All publication charges for this article have been paid for by the Royal Society of Chemistry

Received 21st May 2022
Accepted 18th July 2022

DOI: 10.1039/d2sc02852b

rsc.li/chemical-science

The smallest 4f-metalla-aromatic molecule of cyclo-PrB_2^- with Pr–B multiple bonds†‡

Zhen-Ling Wang,§[a] Teng-Teng Chen,§[b] Wei-Jia Chen,[b] Wan-Lu Li,[a] Jing Zhao,[a] Xue-Lian Jiang,[c] Jun Li,[c] Lai-Sheng Wang *[b] and Han-Shi Hu *[a]

The concept of metalla-aromaticity proposed by Thorn–Hoffmann (*Nouv. J. Chim.* 1979, 3, 39) has been expanded to organometallic molecules of transition metals that have more than one independent electron-delocalized system. Lanthanides, with highly contracted 4f atomic orbitals, are rarely found in multiply aromatic systems. Here we report the discovery of a doubly aromatic triatomic lanthanide-boron molecule PrB_2^- based on a joint photoelectron spectroscopy and quantum chemical investigation. Global minimum structural searches reveal that PrB_2^- has a C_{2v} triangular structure with a paramagnetic triplet $^3B_2$ electronic ground state, which can be viewed as featuring a trivalent Pr(III,f^2) and B_2^{4-}. Chemical bonding analyses show that this cyclo-PrB_2^- species is the smallest 4f-metalla-aromatic system exhibiting σ and π double aromaticity and multiple Pr–B bonding characters. It also sheds light on the formation of the rare B_2^{4-} tetraanion by the high-lying 5d orbitals of the 4f-elements, completing the isoelectronic B_2^{4-}, C_2^{2-}, N_2, and O_2^{2+} series.

1 Introduction

The concept of aromaticity and its role in stabilizing molecules, clusters and materials have been well developed in chemistry. Classical aromaticity usually refers to delocalized (p–p)π systems in unsaturated cyclic hydrocarbons such as benzene. In recent years, the concept of multiple aromaticity has been developed, which involves multiple independent delocalized electron systems (σ, π, δ, or even φ) coexisting in the same molecular systems. The first molecule with σ + π double aromaticity was observed in $C_6H_3^+$ in 1979.[1] In the same year, a seminal paper by Thorn and Hoffmann[2] introduced transition metals into the field of aromaticity, which broadened the scope of this subject into "metalla-aromatic chemistry". In this scenario, a carbon atom of an aromatic hydrocarbon is substituted by a transition metal atom, such that the bonding situation changes into a (d-p)π system. Since then, numerous transition metal compounds with metalla-aromaticity have been synthesized.[3,4] Additionally, many metal clusters have been found to be multiply aromatic, *e.g.*, $Mo_3S_4^{4+}$, Al_4^{2-}, Li_3^+, Hg_4^{6-}, $Ta_3O_3^-$, Hf_3, and $U_4(NH)_4$.[5–16] However, organolanthanide systems with metalla-aromaticity are rare because the 5d orbitals of lanthanides are energetically too high, while the 4f orbitals are radially too contracted to participate in effective bonding with carbon-based ligands.

Compared with its carbon neighbour, the electron-deficient boron element possesses higher 2p-orbital energy and larger 2s-2p orbital radii than carbon,[17,18] which favours efficient bonding with energetically high-lying 5d orbitals of lanthanides, as exemplified by a number of lanthanide boride materials.[19] Joint photoelectron spectroscopy (PES) and quantum chemical studies have shown that size-selected anionic boron clusters (B_n^-) are planar or quasi-planar up to B_{38}^-.[20] All the planar boron clusters feature multi-centre delocalized σ and π bonds over the boron plane, which is a direct consequence of boron's electron efficiency.[21–25] These delocalized σ and π bonds give rise to multiple aromaticity, which stabilizes the planar structures and leads to the concept of all-boron analogues (*e.g.* borophene) of polycyclic aromatic hydrocarbons.[23] Metal-doped boron clusters have recently become a new direction in the study of boron chemistry. It has been discovered that transition metals can be doped into the plane of boron clusters due to the strong metal–boron bonding.[26–28] The d AOs of transition metals are found to participate in electron delocalization in doped planar boron clusters, resulting in the discovery of aromatic metal-centred borometallic wheels, $M©B_n^-$ (n = 8–10).[29–34] Very recently, it has been shown that the Re atom can be

[a]*Department of Chemistry & Key Laboratory of Organic Optoelectronics and Molecular Engineering of the Ministry of Education, Tsinghua University, Beijing, 100084, China. E-mail: hshu@mail.tsinghua.edu.cn*

[b]*Department of Chemistry, Brown University, Providence 02912, Rhode Island, USA. E-mail: Lai-Sheng_Wang@brown.edu*

[c]*Department of Chemistry, Southern University of Science and Technology, Shenzhen 518055, China*

† Dedicated to Professor Dr W. H. E. Schwarz on his 85th birthday.

‡ Electronic supplementary information (ESI) available. See https://doi.org/10.1039/d2sc02852b

§ These authors contributed equally to this work.

positioned on the edge of small planar boron clusters, resulting in the realization of the first cyclic Mobius aromatic metalla-borocycle in ReB_4^- (ref. 35) and the metalla-benzene of ReB_6^-.[36]

Lanthanides (Ln = La–Lu) are a distinct group of elements in the Periodic Table in terms of chemical bonding. On the one hand, they have rather contracted and low-energy 4f AOs that can hardly participate in covalent bonding due to the quantum primogenic effect.[37] On the other hand, promoting electrons from 4f to high-lying 5d AOs requires significant energies even though their 5d AOs can contribute to chemical bonding because of apt radial extension.[38] Thus, the covalent bonding capability of lanthanides is rather limited in comparison with transition metals, especially in their participation in electron delocalization and multiple bonding. It is rare to find f-block atoms in aromatic systems,[8,39–41] let alone multiple aromaticity. A representative case is the triangular La_3^- molecule, which is shown to display σ + π double aromaticity formed by 5d orbitals.[42,43] While compounds with multiple bonds between lanthanides and main group elements, such as Ln=C, Ln=N, and Ln=O,[44,45] have been synthesized,[46,47] Ln–B multiple bonds have been rarely studied so far.[40] Yet recent studies on lanthanide boride clusters have discovered some new structures like half-sandwiches,[48] inverse sandwiches,[49–51] inverse triple-deckers,[52] and spherical trihedral cages,[53] very different from transition metal borides. In most of these systems, the lanthanide atoms interact with a large boron moiety to form delocalized multi-centred chemical bonds, resulting in Ln–B bonds with average bond orders smaller than one.

Here we report a PES and quantum chemical investigation of the triatomic PrB_2^- molecule, which is found to have a cyclo-triangular C_{2v} structure with double σ and π aromaticity. This molecule can be viewed as a trivalent Pr(III,f^2) coordinated by a so-far unidentified B_2^{4-} ligand. Chemical bonding analyses show that this triatomic system is the smallest metalla-aromatic ring containing a magnetic lanthanide atom and two Pr–B multiple bonds.

2 Experimental and computational methods

2.1. Experimental methods

The experiment was carried out using a magnetic-bottle PES apparatus coupled with a laser vaporization supersonic cluster source and a time-of-flight mass spectrometer.[54,55] Briefly, the PrB_2^- anion was generated by laser ablation of a Pr–B disc target prepared by cold-pressing a mixed powder of Pr and ^{11}B (97% enriched). Clusters formed in the nozzle were entrained by a He carrier gas seeded with 10% argon, undergoing a supersonic expansion. A series of PrB_n^- clusters were produced and the PrB_2^- of current interest was mass-selected, decelerated, and then photodetached by the 193 nm (6.424 eV) radiation from an ArF excimer laser and the third harmonics (355 nm, 3.496 eV) from an Nd:YAG laser. The photoelectron spectra were calibrated using the known transitions of Bi^-. The energy resolution of the apparatus was about 2.5%, that is, ~25 meV for 1 eV electrons.

2.2. Computational methods

Quantum chemical calculations were performed by using ADF 2019.1,[56,57] Molpro 2018,[58] and Gaussian 16 programs.[59] Unless otherwise specified, ADF calculations were done at PBE0/TZP level[60,61] with scalar relativistic ZORA correction[62] and 1s–4d electrons frozen for Pr; Gaussian calculations were performed with PBE0 functional and quasi-relativistic effective core potential (ECP) of MWB28 used for Pr,[63,64] together with MWB28 basis set for Pr and the cc-pVTZ basis set[65] for light elements; Molpro calculations utilized MWB28 ECP and MWB28_ANO basis set for Pr, and the cc-pVTZ basis set for B.

Global geometry minimum searches for PrB_2^- were carried out by ADF 2019.1, with three chemically reasonable starting states (linear Pr–B–B, C_s triangle, and C_{2v} triangle) and different spin multiplicities. A C_{2v} triangle with $^3B_2$ electronic state is the global minimum. We also performed two confirmative geometry optimizations for PrB_2^- using the optimized triplet C_{2v} triangle as an initial guess: using ADF with non-collinear ZORA spin–orbit coupling correction,[66] and using Gaussian with DKH2 relativistic Hamiltonian,[67,68] PBE0 functional, SARC-DKH2 basis set for Pr,[69] and cc-pVTZ basis set for B. The neutral PrB_2 was optimized by ADF at doublet and quartet spin states. PBE0 geometries were used for all following calculations. CASSCF-(14o, 12e) calculations were performed by Molpro to verify the reliability of those DFT methods. To compared with the PES, the adiabatic detachment energy (ADE) and the first vertical detachment energy (VDE_1) were calculated at SAOP/TZP level[70] without a frozen core by ADF and at CCSD(T) level by Molpro. TDDFT excitation energies of PrB_2 were added to VDE_1 to obtain higher VDEs, and those calculations were carried out by ADF at SAOP/TZP level, with no frozen core used. Atomic valence-orbital radial-densities of Pr and B were calculated by ADF 2019.1 with PBE functional.[71] The broken spin state was also computed by ADF with care.

Most calculations related to magnetic properties of PrB_2^-, including electron localization function (ELF), diamagnetic anisotropy,[72] nucleus independent chemical shift (NICS),[73] and the input for AICD and GIMIC program,[74,75] were obtained through Gaussian. Those calculations were done properly at the triplet state and as the molecule is not fully symmetric, we picked the centre of the induced-current at 1.5 a_0 above the molecule plane (Fig. 6(b), coordinates in Table S5‡) as the centre of NICS and integrated ring-current[76] calculations. Ring-current integrating planes reach that centre and are orthogonal to the intersected chemical bonds. For readers' reference, NICS values and the GIMIC current strengths were also computed by BHandHLYP and B3LYP functionals.[77,78] The ADF code was used to calculate NICS values with noncollinear spin–orbit effect and a TZP all-electron basis set. These magnetic properties were also computed for two reference molecules, B_3^- and $C_3H_3^+$, at the same level.

For further discussions on chemical bonding, we performed an energy decomposition analysis from the natural orbitals for

chemical valence[79] (EDA-NOCV) by ADF, a principal interaction orbital analysis[80] (PIO) by Gaussian 16 and the PIO package, and an adaptive natural density partitioning analysis[81] (AdNDP) by Gaussian 16 and Multiwfn 3.6,[82] all on PrB_2^-. Bond orders of PrB_2^- were computed by ADF, including Mayer, Gopinathan–Jug, and Nalewajski–Mrozek indices.[83–86]

3 Results and discussions

3.1. Photoelectron spectrum

The 355 nm spectrum of PrB_2^- (Fig. 1(a)) exhibits a sharp and intense ground-state detachment transition (X), yielding an adiabatic detachment energy (ADE) of 1.72 eV, which is also the electron affinity (EA) of neutral PrB_2. A closely-spaced band A at 1.90 eV is observed at 355 nm, but less resolved at 193 nm (Fig. 1(b)). Following a small energy gap, a band B at 2.29 eV is observed with a relatively weak intensity at 355 nm, but it becomes the most intense band in the 193 nm spectrum. A weak and broad band C at 3.13 eV is not clearly resolved at 355 nm, but better defined at 193 nm. Beyond band C, the PES signal is almost continuous, and a band D at around 3.9 eV is tentatively labelled for the sake of discussion. The vertical detachment energies (VDEs) of the observed spectral bands for PrB_2^- are given in Table 1, where they are compared with the theoretical results.

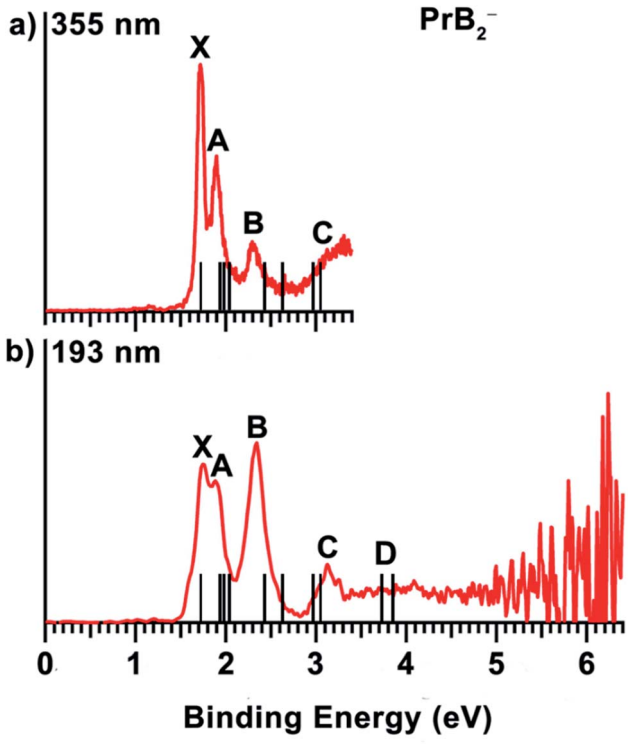

Fig. 1 The photoelectron spectra of PrB_2^- at (a) 355 nm (3.496 eV) and (b) 193 nm (6.424 eV). The vertical bars represent the calculated VDEs (see Table 1).

3.2. Global-minimum structure searches

The triatomic PrB_2^- can take four types of structures: linear Pr–B–B and B–Pr–B, and bent C_s and C_{2v} triangles. The linear B–Pr–B is ruled out because the B–B bond is significantly stronger than the Pr–B bond. Therefore, only the linear Pr–B–B ($C_{\infty v}$), C_s scalene triangle, and C_{2v} unilateral triangle isomers are likely. We conducted systematic geometry optimizations for these initial structures with various electronic states and different spin multiplicities (singlet, triplet, and quintet). It is found that the most stable structure of PrB_2^- within 20 kcal mol^{-1} is the unilateral triangle with C_{2v} symmetry and a triplet $^3B_2$ ground state (Fig. 2). The C_{2v} PrB_2^- consists of a Pr(III) f^2 valence electron configuration and strongly spin-polarized $(\pi_\perp)^2(\pi_\parallel)^2(\sigma_{BB})^2$ bonding orbitals (Fig. 4 and Table S1‡), where $\pi_\perp$ and $\pi_\parallel$ are the out-of-plane (perpendicular) and in-plane components of the B–B π orbitals, respectively. The most stable structure of the neutral PrB_2 molecule with a quartet $^4B_2$ state is found to be similar in structure to that of the PrB_2^- anion with very little structural change (Fig. 2), which is 15 kcal mol^{-1} below any doublet state of the neutral. There is a small decrease of the B–B bond length and a small increase of the Pr–B bond length in neutral PrB_2. The calculated bond lengths and bond angles are given in Fig. 2.

3.3. Comparison between the experimental and computational results

The electronic structures of PrB_2^- and PrB_2 are calculated using several methods of density functional theory (DFT) and wavefunction theory (WFT). More computational details are given in the ESI‡. We have computed the ADE and VDEs of PrB_2^- to compare with the experimental photoelectron spectra (Fig. 1). The VDEs were calculated using the ΔSCF-TDDFT approach.[87,88] Based on the optimized geometry of the PrB_2^- anion and time-dependent DFT, vertical excitation energies of PrB_2 are added to the first VDE (VDE_1) to obtain higher VDEs.

Single-configurational DFT at the PBE0/TZP level using ADF code and CCSD(T) calculations using MOLPRO code with the Stuttgart ECP28MWB effective core potential (ECP) for Pr, the cc-pVTZ basis set for B, and SDD basis set for Pr yielded VDE_1/ADE of 1.52/1.37 eV and 1.50/1.41 eV, respectively. For better comparison with experiment, we systematically shifted the predicted VDEs in Table 1 to align the calculated VDE_1 value with band X. Multi-configurational CASSCF calculations (Fig. S1, S2, and Tables S2, S3 in ESI‡) indicate that the multi-electron wavefunctions of PrB_2^- and PrB_2 are both dominated by a single configuration with the configuration-interaction (CI) weights of 79.6% and 82.1%, respectively, while all other configurations each contributes less than 2%. Thus, these systems can be approximately described by single-configurational methods such as DFT and CCSD(T).

As shown in Table 1, the VDE_1 of X band is derived from removing the β electron from the $6a_1$ molecular orbital (MO), while the next band A corresponds to three detachment channels: $5a_1\beta$, $7a_1\alpha$, and $6a_1\alpha$. Band B comes from the electron removal from the $2b_1$ α- and β-MOs. All X, A and B bands correspond to removing the electrons from the B_2 moiety: the

Table 1 The experimental VDEs for PrB_2^- ($^3B_2$) compared with computational values using the ΔSCF-TDDFT method at the level of SAOP/TZP using ADF code

	VDE (eV) (expt.)	VDE (eV) (comput.)[a]	State	Configuration[b,c]
PrB_2^-			$^3B_2$	$\{...4a_1^2 3b_2^2 2b_1^2\ [5a_1^{\uparrow} 4b_2^{\uparrow}]\ 5a_1^{\downarrow} 6a_1^{\uparrow} 7a_1^{\uparrow} 6a_1^{\downarrow}\}$
X	1.72	1.72	$^4B_2$	$\{...4a_1^2 3b_2^2 2b_1^2\ [5a_1^{\uparrow} 4b_2^{\uparrow}]\ 5a_1^{\downarrow} 6a_1^{\uparrow} 7a_1^{\uparrow} 6a_1^{0}\}$
A	1.90	1.95	$^4B_2$	$\{...4a_1^2 3b_2^2 2b_1^2\ [5a_1^{\uparrow} 4b_2^{\uparrow}]\ 5a_1^{0} 6a_1^{\uparrow} 7a_1^{\uparrow} 6a_1^{\downarrow}\}$
		1.98	$^2B_2$	$\{...4a_1^2 3b_2^2 2b_1^2\ [5a_1^{\uparrow} 4b_2^{\uparrow}]\ 5a_1^{\downarrow} 6a_1^{\uparrow} 7a_1^{0} 6a_1^{\downarrow}\}$
		2.05	$^2B_2$	$\{...4a_1^2 3b_2^2 2b_1^2\ [5a_1^{\uparrow} 4b_2^{\uparrow}]\ 5a_1^{\downarrow} 6a_1^{0} 7a_1^{\uparrow} 6a_1^{\downarrow}\}$
B	2.29	2.42	$^4A_2$	$\{...4a_1^2 3b_2^2 2b_1^{\uparrow}\ [5a_1^{\uparrow} 4b_2^{\uparrow}]\ 5a_1^{\downarrow} 6a_1^{\uparrow} 7a_1^{\uparrow} 6a_1^{\downarrow}\}$
		2.64	$^2A_2$	$\{...4a_1^2 3b_2^2 2b_1^{\downarrow}\ [5a_1^{\uparrow} 4b_2^{\uparrow}]\ 5a_1^{\downarrow} 6a_1^{\uparrow} 7a_1^{\uparrow} 6a_1^{\downarrow}\}$
C	3.13	2.98	$^2B_2$	$\{...4a_1^2 3b_2^2 2b_1^2\ [5a_1^{0} 4b_2^{\uparrow}]\ 5a_1^{\downarrow} 6a_1^{\uparrow} 7a_1^{\uparrow} 6a_1^{\downarrow}\}$
		3.07	$^2A_1$	$\{...4a_1^2 3b_2^2 2b_1^2\ [5a_1^{\uparrow} 4b_2^{0}]\ 5a_1^{\downarrow} 6a_1^{\uparrow} 7a_1^{\uparrow} 6a_1^{\downarrow}\}$
D	~3.9	3.72	$^4A_1$	$\{...4a_1^2 3b_2^{\uparrow} 2b_1^2\ [5a_1^{\uparrow} 4b_2^{\uparrow}]\ 5a_1^{\downarrow} 6a_1^{\uparrow} 7a_1^{\uparrow} 6a_1^{\downarrow}\}$
		3.88	$^2A_1$	$\{...4a_1^2 3b_2^{\downarrow} 2b_1^2\ [5a_1^{\uparrow} 4b_2^{\uparrow}]\ 5a_1^{\downarrow} 6a_1^{\uparrow} 7a_1^{\uparrow} 6a_1^{\downarrow}\}$

[a] The calculated VDEs at the level of SAOP/TZP (at the PBE0 geometry) using ADF code are systematically shifted up by 0.20 eV to align calculated VDE_1 value with band X. [b] "↑" and "↓" in the electron configurations stand for α and β electrons, respectively. [c] The α-MOs $5a_1$ and $4b_2$ mainly arise from quasi-atomic Pr(III, f^2) configuration.

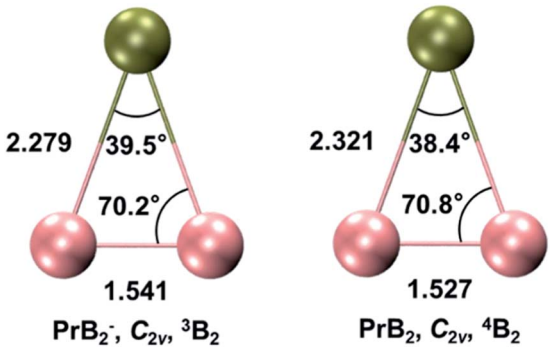

Fig. 2 The global minimum structures of PrB_2^- and PrB_2 calculated at the PBE0/TZP level using ADF program. The bond lengths are given in Å and the bond angles are given in degree (°). Colour codes for atoms: olive–Pr; pink - B.

B–B 2pσ MO and the vertical ($\pi_\perp$) and horizontal ($\pi_\parallel$) B–B 2pπ MOs, which all interact with 6s or 5d orbitals of Pr in an in-plane or out-of-plane fashion (Fig. 4). These bands have relatively high intensities due to the large detachment cross sections of the B 2p orbitals. The fact that the $6a_1\beta$ and $5a_1\beta$ electrons are detached before $7a_1\alpha$ and $6a_1\alpha$ is due to the favoured exchange interaction with the paramagnetic, quasi-atomic Pr f^2 configuration. Detachments of the 4f electrons in the singly occupied molecular orbitals (SOMOs), $5a_1$ and $4b_2$, give rise to band C, which has relatively low intensity. Electron detachment from $3b_2$ α- and β-MOs derived from the B–B σ^*_{2s} antibonding orbital (Fig. 4) account tentatively for the signals near 3.9 eV of band D. When an electron is detached from a doubly occupied MOs (α- and β-MOs with little spin polarization), it can result in either a doublet or quartet final state. Since the quartet state has a higher exchange energy, its VDE is usually lower than its doublet counterpart, as one can see in bands B and D. It should also be noted that, as is common in strongly correlated f-systems,[89,90] generalized Koopmans' theorem (GKT) is violated even qualitatively, making it difficult to assign PES transitions based on GKT with simple Kohn–Sham (K–S) MO energies without calculating the actual initial and final state energies of the electron detachment process. Overall, considering the complicated electron correlation and limited basis sets, the calculated VDEs from ΔSCF-TDDFT approach agree well with the experimental data, confirming the C_{2v} global minimum structure and the ground state of PrB_2^-.

3.4. The electronic structure and chemical bonding of PrB_2^-

Systematic theoretical analyses have been performed to gain insights into the electronic structure and chemical bonding of PrB_2^-. Fig. 3 depicts the radial distribution probability $D(r) = r^2R(r)^2$ of the Pr^{3+} 5d and 4f orbitals as well as the B 2s and 2p orbitals lying at 2.3 Å (the average Pr–B distance in PrB_2^- and PrB_2). The Pr 4f is much more contracted (r_{max} ~0.34 Å) than the 5d orbitals (r_{max} ~1.03 Å) in the radial distribution, leading to nearly negligible orbital overlap between Pr 4f and B 2s/2p. In contrast, the Pr 5d orbitals have significant orbital overlap with B 2s/2p, which accounts for the covalent bonding interaction between Pr 5d and B 2s-2p hybrid orbitals. It is worth noting that B 2p orbitals are radially quite contracted because of the quantum primogenic effect.[91] As a result, both the 2p and 2s orbitals of B atom can overlap with Pr 5d orbitals.

Fig. 4 presents the schematic energy-level correlation diagram between the presumed fragments Pr and B_2^-. From group theory, with molecular plane σ_{yz} of C_{2v} symmetry, the Pr AOs transform as 6s (a_1) as well as $5d_z2$ (a_1), $5d_{xz}$ (b_1), $5d_{yz}$ (b_2), $5d_{xy}$ (a_2) and $5d_{x^2-y^2}$ (a_1), respectively. As shown in Fig. 3, the Pr 4f orbitals are too contracted to overlap with B_2 ligand orbitals, so they span a narrow band consisting of $4f_z3$ (a_1), $4f_{xz}2$ (b_1), $4f_{yz^2}$ (b_2), $4f_{xyz}$ (a_2), $4f_{z(x^2-y^2)}$ (a_1), $4f_{x(x^2-y2)}$ (b_1), $4f_{y(x^2-y^2)}$ (b_2), with the $5a_1$ and $4b_2$ α-MOs occupied in the f^2 electron configuration. As the B($2s^22p^1$) atom has three valence electrons, from the well-known Mulliken qualitative MO levels of diatomic molecule (Fig. 4), one can obtain the familiar

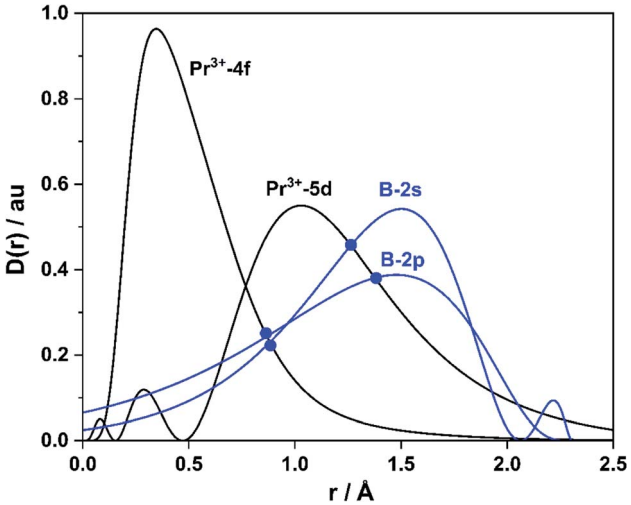

Fig. 3 Atomic valence-orbital radial-densities $D(r) = r^2R(r)^2$ of 4f/5d orbitals (black lines) of Pr^{3+} ion with $4f^2$ configuration and of 2s/2p orbitals (blue lines) of B atom lying at 2.3 Å (from PBE density functional calculations).

$(\sigma_{2s})^2(\sigma^*_{2s})^2(\pi_{2p})^2(\sigma_{2p})^1(\pi^*_{2p})^0(\sigma^*_{2p})^0$ electron configuration for B_2^- ion, where 2s/2p indicating the composing atomic orbitals (AOs) and asterisk (*) denotes antibonding MOs.

In Fig. 4, σ_{2s} of B_2^- is rather low in energy compared with the valence AOs of Pr; therefore, it participates weakly in bonding with 6s as well as $5d_{z^2}/5d_{x^2-y^2}$ when Pr is coordinated by B_2^-. However, as the size of B 2s is as large as the 2p orbitals based on the radial distribution function (Fig. 3), B 2s can interact with Pr 5d orbitals when they are not too far apart energetically. Indeed, the antibonding σ^*_{2s} MO in B_2^- forms the bonding $3b_2$ MO upon interaction with Pr $5d_{yz}$ AOs. The two degenerate π_{2p} MOs of B_2^- also interact with the Pr 5d AOs, in two different ways: the π_{2p} MO perpendicular to the molecular plane ($\pi_\perp$) forms a 3c–2e π bonding $2b_1$ MO with Pr $5d_{xz}$ while the π_{2p} MO in the plane of the molecule ($\pi_\parallel$) forms a 3c–2e σ bonding $6a_1$ MO with Pr $5d_{z^2}/5d_{x^2-y^2}$ AOs, as is illustrated in Scheme 1. The σ_{2p} MO of B_2^- is slightly stabilized by interacting with Pr 6s as well as $5d_{z^2}/5d_{x^2-y^2}$ AOs. As a result, the Pr 6s AO has been pushed up significantly by interacting with the σ_{2s} and σ_{2p} MOs of B_2^- with the same symmetry, forming the lowest unoccupied MO (4σ). Overall, the orbital interaction between σ_{2p} and π_{2p} MOs of B_2^- and Pr 5d/6s AOs leads to significant bonding stabilization of $\pi_\perp$, $\pi_\parallel$, and 3σ MOs of PrB_2^-, which causes Pr to lose three electrons to fill the B-2p based MOs to form the electron configuration of $(\pi_\perp)^2(\pi_\parallel)^2(\sigma_{BB})^2$ $Pr^{III}(4f^26s^0)$. Therefore, the PrB_2^- molecule can be described as composed of a +3-oxidation-state Pr^{3+} (*i.e.*, Pr^{III}) with f^2-configuration and formally a coordinated B_2^{4-} tetraanion, namely $Pr^{III}[B_2^{4-}]$. Interestingly, the B_2^{4-} tetraanion is isoelectronic with the C_2^{2-}, N_2, and O_2^{2+} diatomic moiety that has the well-known $(\sigma_{2s})^2(\sigma^*_{2s})^2(\pi_{2p})^4(\sigma_{2p})^2(\pi^*_{2p})^0(\sigma^*_{2p})^0$ electron configuration, despite the much higher σ_{2p} and π_{2p} orbital energies of B_2^{4-} due to smaller electronegativity of B than C, N and O. The spin-polarized α and β sets of MOs and the contour surfaces of the PrB_2^- valence MOs are shown in Table 2. Therefore, there are five sets of interactions among the three atoms of PrB_2^-, including the α + β sets of $4a_1$, $3b_2$, $2b_1$, as well as the more spin polarized $6a_1\alpha + 6a_1\beta$ and $7a_1\alpha + 5a_1\beta$.

It should be noted that the nearly degenerate 4f MO levels are stabilized in Pr(III) and slightly split due to the presence of B_2^-, similar to the crystal field splitting. As a result, the lowest energy state corresponds to the two 4f electrons staying in two specific 4f MOs, *i.e.*, the $5a_1\alpha$ and $4b_2\alpha$ sets, forming a paramagnetic ground state. The calculated magnetic exchange coupling constant $J = -\dfrac{E_{HS} - E_{BS}}{\langle\hat{S}^2\rangle_{HS} - \langle\hat{S}^2\rangle_{BS}} = 6703\ cm^{-1}$, where E_{HS} and E_{BS} are the energies of the triplet high-spin (HS) and broken-symmetry (BS) singlet states. However, in DFT calculations, due to the self-interaction error (SIE)[92] and hybrid mixing of Hartree–Fock exchange, virtual 4f orbitals are much higher in energy, resulting in only two occupied 4f α-MOs having relatively low energies.

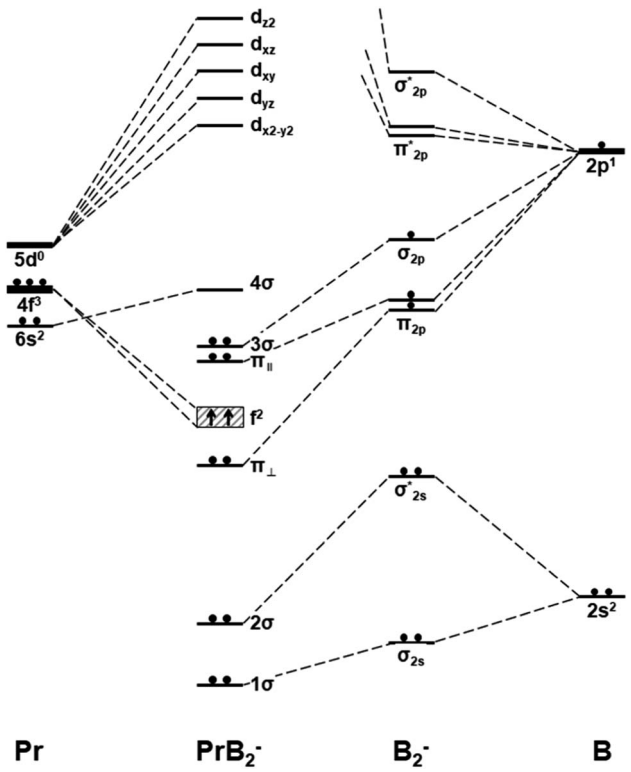

Fig. 4 Schematic orbital energy levels of triangle $Pr(\eta_2\text{-}B_2)^-$, B_2^-, and Pr. The symbol $\pi_\parallel$ and $\pi_\perp$ denotes the in-plane and out-of-plane π MOs, and their respective orbital interaction with Pr $5d_{x^2-y^2}$ and $5d_{xz}$ orbitals are shown in Scheme 1.

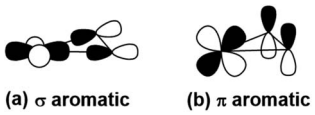

Scheme 1 The σ-type and π-type orbital interaction between Pr-5d and B-2p orbitals, leading to (a) σ- and (b) π- metalla-aromaticity, respectively.

Table 2 The spin-polarized α and β set Kohn–Sham MOs of PrB_2^- calculated at the PBE0/TZP level using ADF code. Colour codes: olive – Pr; pink – B

α – MO					β – MO				
Kind	Irrep.	$-\varepsilon_i$ (eV)	MO% (Pr : B_2)	Contour	Kind	Irrep.	$-\varepsilon_i$ (eV)	MO% (Pr : B_2)	Contour
3σ	$7a_1$	1.78	70 : 30	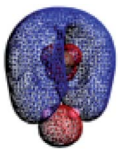	3σ	$5a_1$	1.97	44 : 56	
$\pi_{\parallel}$	$6a_1$	1.90	37 : 63	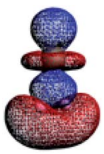	$\pi_{\parallel}$	$6a_1$	1.77	40 : 60	
f^2	$4b_2$	2.26	97 : 3	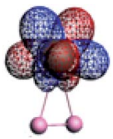					
f^2	$5a_1$	2.33	91 : 9						
$\pi_{\perp}$	$2b_1$	2.46	38 : 62		$\pi_{\perp}$	$2b_1$	2.43	33 : 67	
2σ	$3b_2$	3.95	36 : 64	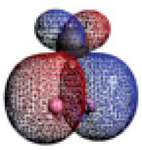	2σ	$3b_2$	4.00	26 : 74	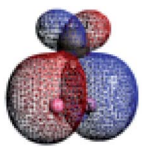
1σ	$4a_1$	9.26	16 : 84	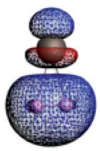	1σ	$4a_1$	9.35	15 : 85	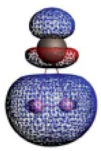

Interestingly, the linear Pr–B–B isomer shares a similar bonding pattern with the C_{2v} global minimum (Fig. S4–S5 and Table S7‡). The σ_{2s} MO is still too low in energy to be bonded with Pr, and the bonding 6σ MO is formed by σ^*_{2s}. The two π_{2p} MOs in B_2^- form a pair of degenerate π bonding MOs with Pr 5d AOs. Also, the 6s AO in Pr is now non-bonded and occupied in the 7σα MO, while σ_{2p} interacts with a 5d AO forming a 7σβ bonding MO. The Pr oxidation state of this linear isomer is thus +2. As the 6s electron is unpaired, the total bonding interaction in the linear structure is weaker than that in the triangle structure, implying that a linear PrB_2^- would tend to bend into a triangle arrangement by the second-order Jahn–Teller effect.[93]

The global minimum of PrB_2^- is found to be doubly aromatic, as verified by various analyses including the canonical K–S MOs, adaptive natural density partitioning[81] (AdNDP) analysis, induced ring-current strength,[76] the anisotropy of the induced current density[75] (AICD), the diamagnetic anisotropy,[72] the nucleus-independent chemical shift (NICS)[73] and the bifurcation analysis of electron localization function (ELF) of the σ and π electrons.[94] In the K–S MOs, there are two delocalized 3c–2e MOs consisting of Pr and B_2 moity: a σ bonding MO of $6a_1$ and a π bonding MO of $2b_1$. These two delocalized 3c–2e bonding MOs of $6a_1$ and $2b_1$ in Table 2 can also be verified by the AdNDP results (Fig. 5), where the first row describes three localized σ bonds and the

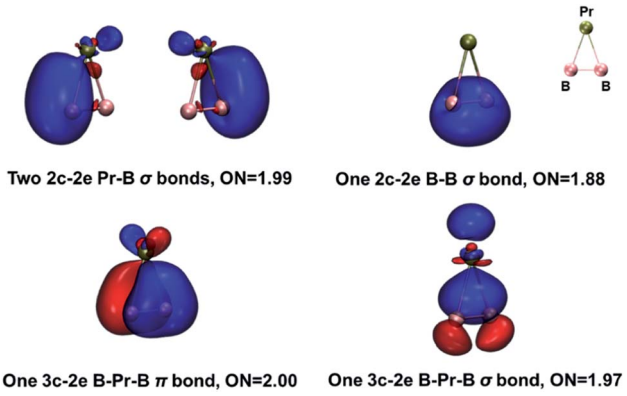

Fig. 5 Results of the AdNDP analysis on PrB_2^- using the Gaussian-16 program. The occupation numbers are given as ON values. Isovalue = 0.05 for all orbitals; colour codes for atoms: olive, Pr; pink, B.

second row represents delocalized σ and π bonds within the PrB_2 framework. Therefore, PrB_2^- has two independent delocalized systems each containing two electrons, satisfying the $4n + 2$ Hückel rule ($n = 0$) and giving rise to double σ + π aromaticity. The delocalized π bonding is similar to that in [Sc]C_2RR′, a metalla-cyclopropene reported by Zhang *et al.*[95] and that in LaB_2^- and LaB_3 molecules.[40]

Aromaticity is a useful concept despite its many facets. NICS values are often used to assess aromaticity because the negative value of the diamagnetic anisotropy suggests delocalization, also consistent with its aromaticity. Albeit being widely used, the NICS values may be artificially lowered by the local paramagnetic current around the Pr nucleus in PrB_2^-, thus may give negative values even if a global ring-current is non-existent and fail to assess aromaticity in some metallic systems.[96–100] However, the NICS values can still help to provide helpful information about aromaticity when combining with other criteria. $NICS_{zz}(\zeta)$ (the out-of-plane component of the chemical shift tensor calculated at ζ distance above the molecular plane) of PrB_2^- and two reference molecules (the singly π aromatic $C_3H_3^+$ and the doubly σ + π aromatic B_3^-) are compared in Table S8.‡ Although in the literature,[101,102] the ring critical point is the common point for calculating NICS values, PrB_2^- does not have one and as the molecule is less symmetric compared with B_3^- and $C_3H_3^+$, the centre of the ring current (Fig. 6(b), coordinates in Table S5‡) is used instead of the geometry centre. The NICS values calculated both at the scalar relativistic and spin–orbit coupling relativistic levels of theory are listed in Tables S8(a) and (b),‡ as long as it would be ideal to include the spin–orbit coupling effect, which has been proved to influence NICS and ring-current values.[103–106] One can see that the $NICS_{zz}(\zeta)$ originating from the π-aromatic ring in $C_3H_3^+$ remains almost the same as ζ increases from 0 to 1 because the π bonding MOs are perpendicular to the molecular plane. Comparatively, the $NICS_{zz}(\zeta)$ values of the doubly σ + π aromatic B_3^- and PrB_2^- molecules decreases more significantly as ζ increases, which is because of the delocalized in-plane σ bond. The large negative $NICS_{zz}$ values of PrB_2^- in comparison with those of $C_3H_3^+$ and B_3^- further help to confirm its double aromaticity.

Table 3 Integrated induced ring-current (in nA/T) passing the B–B bond and diamagnetic anisotropy (in a.u.) of PrB_2^- and B_3^-, computed by the Gaussian −16 program with MWB28 ECP and basis set for Pr and cc-pVTZ basis set for B. A positive value of the ring-current indicates the existence of a diatropic induced current

	B_3^-	PrB_2^-
Integrated ring-current	16.5	7.0
Diamagnetic anisotropy	−5.9	−22.0

In addition, due to the cyclic electron delocalization, when applying a magnetic field to a molecule, a global diamagnetic induced ring-current also suggests aromaticity. Therefore, we have calculated the integrated amount of the induced current, using the same centre as the NICS calculations, passing along the B–B bond. As listed in Table 3, the results indicate that PrB_2^- is magnetically aromatic. Fig. 6 represents the line integral convolution (LIC) visualization of the induced current PrB_2^-. The small clockwise current in (a) can be attributed to the delocalized σ bond, and the global clockwise current in (b) results from the delocalized π bond. The clockwise global diamagnetic currents are diatropic and clear, providing support for the double aromaticity of PrB_2^-. Fig. S6‡ also presents the isosurfaces of AICD of B_3^- and PrB_2^- calculated from all valence electrons for the delocalized σ MO and the delocalized π MO. The isosurfaces decorated by green arrows show the strength and the direction of the induced current, which shows that apart from the counter-clockwise paramagnetic current on Pr, there also exists a global diamagnetic ring-current for PrB_2^- in all three cases, supporting double aromaticity. The connected isosurface of AICD and the bifurcation analysis of ELF (Fig. S7‡) both indicate that the relevant σ and π electrons in PrB_2^- are well delocalized, providing another proof that PrB_2^- is doubly aromatic.

We have also carried out an energy decomposition analysis from the natural orbitals for chemical valence[79] (EDA-NOCV, Table S10‡) and the principal interaction orbital analysis[80] (PIO, Fig. S8‡) to illustrate the bonding pattern between Pr and B_2^-. Both the EDA-NOCV and PIO results suggest four significant sets of orbital interactions between Pr and B_2^-. The AdNDP analysis (Fig. 5) shows three peripheral 2c-2e σ bond in PrB_2^-, in addition to the 3c–2e σ bond and 3c–2e π bond. Therefore, the bond order of the Pr–B bond can be viewed roughly as $1 + (1/3) \times 2 = 5/3$, indicating multiple Pr–B bond character. The bonding in PrB_2^- is identical to that in the smallest doubly aromatic boron cluster, B_3^-, which has also been suggested to

Table 4 Calculated Mayer, Gopinathan–Jug and Nalewajski–Mrozek bond order indices of PrB_2^- by using PBE0/TZP

Type	Mayer	G-J[a]	N-M (1)[b]	N-M (2)[b]	N-M (3)[b]
Pr–B	1.92	1.31	1.97	2.36	1.94
B–B	1.56	2.44	2.31	1.05	2.88

[a] Gopinathan–Jug bond orders. [b] Nalewajski–Mrozek bond orders.

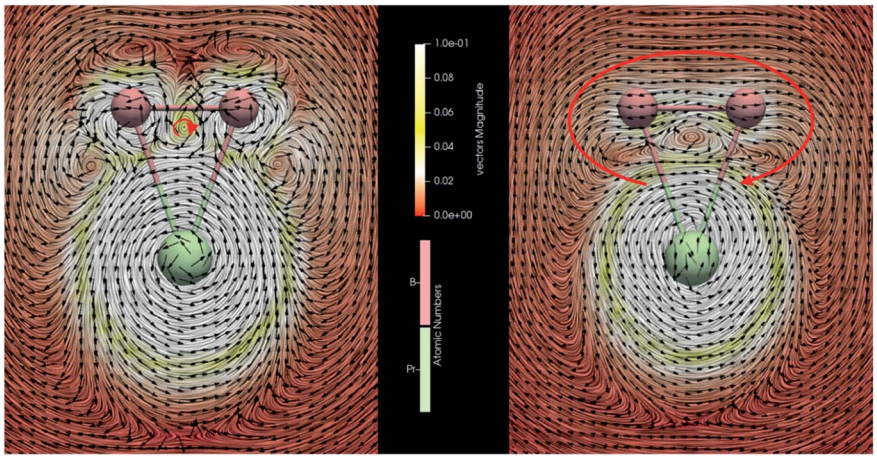

Fig. 6 The strength and direction of the induced current of PrB_2^- at (a) the molecular plane and (b) 1.5 a.u. above the molecular plane calculated by the GIMIC program with MWB28 ECP and basis set for Pr and cc-pVTZ basis set for B. The magnetic field is pointing out of the molecule plane. Black arrows indicate the direction of the current. Clockwise currents represented by red arrows are diatropic and indicate aromaticity.

have a 5/3 bond order by Kuznetsov and Boldyrev.[107] Finally, the five types of bond order indices[83–86] listed in Table 4 reveal that both Pr–B interactions in PrB_2^- have a bond order greater than one, consistent with the Pr–B multiple bond character. Interestingly, both the Gopinathan–Jug bond order and the Nalewajski–Mrozek bond orders support the assignment of triple B≡B bond in the B_2^{4-} tetraanion, similar to the isoelectronic N≡N.

4 Conclusion

In summary, we report a photoelectron spectroscopy and quantum chemistry study of PrB_2^-, which is found to have a C_{2v} unilateral triangle structure with a paramagnetic triplet ground state $^3B_2$. The Pr atom is shown to lose three electrons to form the trivalent Pr(III) with f^2 configuration and an unprecedented B_2^{4-} tetraanion, which is in contrast to the PrB_x^- (x = 3, 4) clusters with Pr(II) and B_3^{3-} as well as Pr(I) and B_4^{2-}, respectively.[108] The π orbitals of the B≡B triple bonds in B_2^{4-} participate in bonding with Pr^{III}, forming an in-plane σ-type and out-of-plane π-type three-centred delocalized systems (Scheme 1) and giving rise to double aromaticity involving a 4f metal atom. The localized peripheral Pr–B σ-bond plus the two 3c–2e delocalized bonds results in multiple bond characters for the Pr–B bonds. The current study demonstrates that metalla-aromaticity and multiple chemical bonds between 4f metals and boron are viable and broadens the chemistry between lanthanide and boron. The present work also reveals that the high-lying 5d orbitals of the 4f-elements can facilitate the formation of the B_2^{4-} tetraanion, which complete the isoelectronic B_2^{4-}, C_2^{2-} and N_2 and O_2^{2+} series.[109,110] The insight of the characteristic high-lying 5d orbitals of the 4f-elements can provide guidance in preparing organometallic complexes with highly negatively charged organic ligands of rare-earth elements.[111,112]

Data availability

The data that supports the findings of this study is available from the corresponding author upon reasonable request.

Author contributions

H. S. H. and L. S. W. designed the project. T. T. C. and W. J. C. performed the experiments. Z. L. W., W. L. L., J. Z., and X. L. J. performed the computational calculations. Z. L. W., T. T. C., J. L., L. S. W. and H. S. H. wrote and edited the manuscript. All authors helped to analyse the experimental and theoretical results.

Conflicts of interest

The authors declare no conflict of interest.

Acknowledgements

The experiment done at Brown University was supported by the National Science Foundation (CHE-2053541). The theoretical work was supported by the National Natural Science Foundation of China (Grant No. 21906094, 22076095, 22033005) and the support of Guangdong Provincial Key Laboratory of Catalysis (No. 2020B121201002). The calculations were done using supercomputers at Tsinghua National Laboratory for Information Science and Technology, and the Computational Chemistry Laboratory of the Department of Chemistry under the Tsinghua Xuetang Talents Program.

References

1 J. Chandrasekhar, E. D. Jemmis and P. von Ragué Schleyer, Double Aromaticity: Aromaticity in Orthogonal Planes. The

3,5-Dehydrophenyl Cation, *Tetrahedron Lett.*, 1979, **20**(39), 3707–3710, DOI: 10.1016/S0040-4039(01)95503-0.

2 D. L. Thorn and R. Hoffman, Delocalization in Metallacycles, *Nouv. J. Chim.*, 1979, **3**, 39–45.

3 D. Chen, Y. Hua and H. Xia, Metallaaromatic Chemistry: History and Development, *Chem. Rev.*, 2020, **120**(23), 12994–13086, DOI: 10.1021/acs.chemrev.0c00392.

4 I. Fernández, G. Frenking and G. Merino, Aromaticity of Metallabenzenes and Related Compounds, *Chem. Soc. Rev.*, 2015, **44**(18), 6452–6463, DOI: 10.1039/c5cs00004a.

5 A. I. Boldyrev and L. S. Wang, All-Metal Aromaticity and Antiaromaticity, *Chem. Rev.*, 2005, **105**(10), 3716–3757, DOI: 10.1021/cr030091t.

6 D. Y. Zubarev, B. B. Averkiev, H. J. Zhai, L. S. Wang and A. I. Boldyrev, Aromaticity and Antiaromaticity in Transition-Metal Systems, *Phys. Chem. Chem. Phys.*, 2008, **10**(2), 257–267, DOI: 10.1039/b713646c.

7 B. B. Averkiev and A. I. Boldyrev, Hf_3 Cluster Is Triply (σ-, π-, and δ-) Aromatic in the Lowest D_{3h}, $^1A_1'$ State, *J. Phys. Chem. A*, 2007, **111**(50), 12864–12866, DOI: 10.1021/jp077528b.

8 A. C. Tsipis, C. E. Kefalidis and C. A. Tsipis, The Role of the 5f Orbitals in Bonding, Aromaticity, and Reactivity of Planar Isocyclic and Heterocyclic Uranium Clusters, *J. Am. Chem. Soc.*, 2008, **130**(28), 9144–9155, DOI: 10.1021/ja802344z.

9 D. Y. Zubarev and A. I. Boldyrev, Multiple Aromaticity, Multiple Antiaromaticity, and Conflicting Aromaticity in Inorganic Systems, *Encycl. Inorg. Chem.*, 2009, DOI: 10.1002/0470862106.ia633.

10 C. A. Tsipis, Aromaticity/Antiaromaticity in "Bare" and "Ligand-Stabilized" Rings of Metal Atoms, *Structure and Bonding*, ed. Parkin G., Springer Berlin Heidelberg, Berlin, Heidelberg, 2010, vol. 136, pp. 217–274. DOI: 10.1007/978-3-642-05243-9_7.

11 A. P. Sergeeva, B. B. Averkiev, and A. I. Boldyrev, All-Transition Metal Aromaticity and Antiaromaticity, ed. Parkin G., *Structure and Bonding*, Springer Berlin Heidelberg, Berlin, Heidelberg, 2010, vol. 136, pp. 275–305. DOI: 10.1007/978-3-642-05243-9_8.

12 J. Li, C.-W. Liu and J.-X. Lu, Ab Initio Studies of Electronic Structures and Quasi-Aromaticity in $M_3S_{4-n}O^{4+}{}_n$(M = Mo, W; n = 0–4) Clusters, *J. Chem. Soc., Faraday Trans.*, 1994, **90**(1), 39–45, DOI: 10.1039/FT9949000039.

13 X. Li, A. E. Kuznetsov, H.-F. Zhang, A. I. Boldyrev and L.-S. Wang, Observation of All-Metal Aromatic Molecules, *Science*, 2001, **291**(5505), 859–861, DOI: 10.1126/science.291.5505.859.

14 A. N. Alexandrova and A. I. Boldyrev, σ-Aromaticity and σ-Antiaromaticity in Alkali Metal and Alkaline Earth Metal Small Clusters, *J. Phys. Chem. A*, 2003, **107**(4), 554–560, DOI: 10.1021/jp027008a.

15 A. E. Kuznetsov, J. D. Corbett, L.-S. Wang and A. I. Boldyrev, Aromatic Mercury Clusters in Ancient Amalgams, *Angew. Chem., Int. Ed.*, 2001, **40**(18), 3369–3372, DOI: 10.1002/1521-3773(20010917)40:18<3369::AID-ANIE3369>3.0.CO;2-Z.

16 H.-J. Zhai, B. B. Averkiev, D. Y. Zubarev, L. Wang and A. I. Boldyrev, δ Aromaticity in $[Ta_3O_3]^-$, *Angew. Chem., Int. Ed.*, 2007, **46**(23), 4277–4280, DOI: 10.1002/anie.200700442.

17 M. Zhou, N. Tsumori, Z. Li, K. Fan, L. Andrews and Q. Xu, OCBBCO: A Neutral Molecule with Some Boron-Boron Triple Bond Character, *J. Am. Chem. Soc.*, 2002, **124**(44), 12936–12937, DOI: 10.1021/ja026257+.

18 W.-L. Li, H.-S. Hu, Y.-F. Zhao, X. Chen, T.-T. Chen, T. Jian, L.-S. Wang and J. Li, Recent Progress on the Investigations of Boron Clusters and Boron-Based Materials (I): Borophene, *Sci. Sin.: Chim.*, 2018, **48**(2), 98–107, DOI: 10.1360/N032017-00185.

19 T. Mori, Lanthanides: Boride, Carbide, and Nitride Compounds, in *Encyclopedia of Inorganic and Bioinorganic Chemistry*, John Wiley & Sons, Ltd, Chichester, UK, 2012. DOI: 10.1002/9781119951438.eibc2028.

20 T. Jian, X. Chen, S. D. Li, A. I. Boldyrev, J. Li and L. S. Wang, Probing the Structures and Bonding of Size-Selected Boron and Doped-Boron Clusters, *Chem. Soc. Rev.*, 2019, **48**(13), 3550–3591, DOI: 10.1039/c9cs00233b.

21 A. P. Sergeeva, I. A. Popov, Z. A. Piazza, W.-L. Li, C. Romanescu, L.-S. Wang and A. I. Boldyrev, Understanding Boron through Size-Selected Clusters: Structure, Chemical Bonding, and Fluxionality, *Acc. Chem. Res.*, 2014, **47**(4), 1349–1358, DOI: 10.1021/ar400310g.

22 H. J. Zhai, A. N. Alexandrova, K. A. Birch, A. I. Boldyrev and L. S. Wang, Hepta- and Octacoordinate Boron in Molecular Wheels of Eight- and Nine-Atom Boron Clusters: Observation and Confirmation, *Angew. Chem., Int. Ed.*, 2003, **42**(48), 6004–6008, DOI: 10.1002/anie.200351874.

23 H. J. Zhai, B. Kiran, J. Li and L. S. Wang, Hydrocarbon Analogues of Boron Clusters Planarity, Aromaticity and Antiaromaticity, *Nat. Mater.*, 2003, **2**(12), 827–833, DOI: 10.1038/nmat1012.

24 D. Y. Zubarev and A. I. Boldyrev, Comprehensive Analysis of Chemical Bonding in Boron Clusters, *J. Comput. Chem.*, 2007, **28**(1), 251–268, DOI: 10.1002/jcc.20518.

25 A. I. Boldyrev and L.-S. Wang, Beyond Organic Chemistry: Aromaticity in Atomic Clusters, *Phys. Chem. Chem. Phys.*, 2016, **18**(17), 11589–11605, DOI: 10.1039/C5CP07465G.

26 W. Li, T. Jian, X. Chen, T. Chen, G. V. Lopez, J. Li and L. Wang, The Planar CoB_{18}^- Cluster as a Motif for Metallo-Borophenes, *Angew. Chem., Int. Ed.*, 2016, **55**(26), 7358–7363, DOI: 10.1002/anie.201601548.

27 T. Jian, W.-L. Li, X. Chen, T.-T. Chen, G. V. Lopez, J. Li and L.-S. Wang, Competition between Drum and Quasi-Planar Structures in RhB_{18}^- : Motifs for Metallo-Boronanotubes and Metallo-Borophenes, *Chem. Sci.*, 2016, **7**(12), 7020–7027, DOI: 10.1039/C6SC02623K.

28 W.-L. Li, X. Chen, T. Jian, T.-T. Chen, J. Li and L.-S. Wang, From Planar Boron Clusters to Borophenes and Metalloborophenes, *Nat. Rev. Chem.*, 2017, **1**(10), 0071, DOI: 10.1038/s41570-017-0071.

29 C. Romanescu, T. R. Galeev, W.-L. Li, A. I. Boldyrev and L.-S. Wang, Aromatic Metal-Centered Monocyclic Boron Rings: $Co©B_8^-$ and $Ru©B_9^-$, *Angew. Chem., Int. Ed.*, 2011, **50**(40), 9334–9337, DOI: 10.1002/anie.201104166.

30 T. R. Galeev, C. Romanescu, W.-L. Li, L.-S. Wang and A. I. Boldyrev, Observation of the Highest Coordination Number in Planar Species: Decacoordinated Ta©B_{10}^- and Nb©B_{10}^- Anions, *Angew. Chem., Int. Ed.*, 2012, **51**(9), 2101–2105, DOI: 10.1002/anie.201107880.

31 W.-L. Li, C. Romanescu, T. R. Galeev, Z. A. Piazza, A. I. Boldyrev and L.-S. Wang, Transition-Metal-Centered Nine-Membered Boron Rings: M©B_9 and M©B_9^- (M = Rh, Ir), *J. Am. Chem. Soc.*, 2012, **134**(1), 165–168, DOI: 10.1021/ja209808k.

32 C. Romanescu, T. R. Galeev, A. P. Sergeeva, W.-L. Li, L.-S. Wang and A. I. Boldyrev, Experimental and Computational Evidence of Octa- and Nona-Coordinated Planar Iron-Doped Boron Clusters: Fe©B_8^- and Fe©B_9^-, *J. Organomet. Chem.*, 2012, **721–722**, 148–154, DOI: 10.1016/j.jorganchem.2012.07.050.

33 C. Romanescu, T. R. Galeev, W.-L. Li, A. I. Boldyrev and L.-S. Wang, Transition-Metal-Centered Monocyclic Boron Wheel Clusters (M©B_n): A New Class of Aromatic Borometallic Compounds, *Acc. Chem. Res.*, 2013, **46**(2), 350–358, DOI: 10.1021/ar300149a.

34 T.-T. Chen, W.-L. Li, H. Bai, W.-J. Chen, X.-R. Dong, J. Li and L.-S. Wang, Re©B_8^- and Re©B_9^- : New Members of the Transition-Metal-Centered Borometallic Molecular Wheel Family, *J. Phys. Chem. A*, 2019, **123**(25), 5317–5324, DOI: 10.1021/acs.jpca.9b03942.

35 L. F. Cheung, G. S. Kocheril, J. Czekner and L.-S. Wang, Observation of Möbius Aromatic Planar Metallaborocycles, *J. Am. Chem. Soc.*, 2020, **142**(7), 3356–3360, DOI: 10.1021/jacs.9b13417.

36 L. F. Cheung, J. Czekner, G. S. Kocheril and L. S. Wang, ReB_6^-: A Metallaboron Analog of Metallabenzenes, *J. Am. Chem. Soc.*, 2019, **141**(44), 17854–17860, DOI: 10.1021/jacs.9b09110.

37 Y. Tang, S. Zhao, B. Long, J.-C. Liu and J. Li, On the Nature of Support Effects of Metal Dioxides MO_2 (M = Ti, Zr, Hf, Ce, Th) in Single-Atom Gold Catalysts: Importance of Quantum Primogenic Effect, *J. Phys. Chem. C*, 2016, **120**(31), 17514–17526, DOI: 10.1021/acs.jpcc.6b05338.

38 J.-B. Lu, D. C. Cantu, M.-T. Nguyen, J. Li, V.-A. Glezakou and R. Rousseau, Norm-Conserving Pseudopotentials and Basis Sets To Explore Lanthanide Chemistry in Complex Environments, *J. Chem. Theory Comput.*, 2019, **15**(11), 5987–5997, DOI: 10.1021/acs.jctc.9b00553.

39 Y. Luo and Z. Hou, Prediction of Binary Lanthanide(III) Hydride Clusters Ln_nH_{3n} (Ln = La, Gd, and Lu; n = 3 and 4), *J. Phys. Chem. C*, 2008, **112**(2), 635–638, DOI: 10.1021/jp077318z.

40 S.-B. Cheng, C. Berkdemir and A. W. Castleman, Observation of d–p Hybridized Aromaticity in Lanthanum-Doped Boron Clusters, *Phys. Chem. Chem. Phys.*, 2014, **16**(2), 533–539, DOI: 10.1039/C3CP53245C.

41 J. T. Boronski, J. A. Seed, D. Hunger, A. W. Woodward, J. van Slageren, A. J. Wooles, L. S. Natrajan, N. Kaltsoyannis and S. T. Liddle, A Crystalline Tri-Thorium Cluster with σ-Aromatic Metal–Metal Bonding, *Nature*, 2021, **598**(7879), 72–75, DOI: 10.1038/s41586-021-03888-3.

42 X. X. Chi and Y. Liu, Theoretical Evidence of d-Orbital Aromaticity in Anionic Metal X_3^- (X = Sc, Y, La) Clusters, *Int. J. Quantum Chem.*, 2007, **107**(9), 1886–1896, DOI: 10.1002/qua.21326.

43 A. S. Ivanov, X. Zhang, H. Wang, A. I. Boldyrev, G. Gantefoer, K. H. Bowen and I. Černušák, Anion Photoelectron Spectroscopy and CASSCF/CASPT2/RASSI Study of La_n^- (n = 1, 3–7), *J. Phys. Chem. A*, 2015, **119**(46), 11293–11303, DOI: 10.1021/acs.jpca.5b08076.

44 O. T. Summerscales and J. C. Gordon, Complexes Containing Multiple Bonding Interactions between Lanthanoid Elements and Main-Group Fragments, *RSC Adv.*, 2013, **3**(19), 6682–6692, DOI: 10.1039/c3ra23151h.

45 Q. Zhu, J. Zhu and C. Zhu, Recent Progress in the Chemistry of Lanthanide-Ligand Multiple Bonds, *Tetrahedron Lett.*, 2018, **59**(6), 514–520, DOI: 10.1016/j.tetlet.2017.12.079.

46 D. Schädle and R. Anwander, Rare-Earth Metal and Actinide Organoimide Chemistry, *Chem. Soc. Rev.*, 2019, **48**(24), 5752–5805, DOI: 10.1039/c8cs00932e.

47 T. Cheisson, K. D. Kersey, N. Mahieu, A. McSkimming, M. R. Gau, P. J. Carroll and E. J. Schelter, Multiple Bonding in Lanthanides and Actinides: Direct Comparison of Covalency in Thorium(IV)- and Cerium(IV)-Imido Complexes, *J. Am. Chem. Soc.*, 2019, **141**(23), 9185–9190, DOI: 10.1021/jacs.9b04061.

48 T. T. Chen, W. L. Li, T. Jian, X. Chen, J. Li and L. S. Wang, PrB_7^-: A Praseodymium-Doped Boron Cluster with a Pr^{II} Center Coordinated by a Doubly Aromatic Planar η^7-B_7^{3-} Ligand, *Angew. Chem., Int. Ed.*, 2017, **56**(24), 6916–6920, DOI: 10.1002/anie.201703111.

49 W. L. Li, T. T. Chen, D. H. Xing, X. Chen, J. Li and L. S. Wang, Observation of Highly Stable and Symmetric Lanthanide Octa-Boron Inverse Sandwich Complexes, *Proc. Natl. Acad. Sci. U. S. A.*, 2018, **115**(30), E6972–E6977, DOI: 10.1073/pnas.1806476115.

50 T. T. Chen, W. L. Li, J. Li and L. S. Wang, $[La(H_x\text{-}B_x)La]^-$ (x = 7-9): A New Class of Inverse Sandwich Complexes, *Chem. Sci.*, 2019, **10**(8), 2534–2542, DOI: 10.1039/c8sc05443f.

51 Z.-Y. Jiang, T.-T. Chen, W.-J. Chen, W.-L. Li, J. Li and L.-S. Wang, Expanded Inverse-Sandwich Complexes of Lanthanum Borides: $La_2B_{10}^-$ and $La_2B_{11}^-$, *J. Phys. Chem. A*, 2021, **125**(12), 2622–2630, DOI: 10.1021/acs.jpca.1c01149.

52 T. T. Chen, W. L. Li, W. J. Chen, J. Li and L. S. Wang, $La_3B_{14}^-$: An Inverse Triple-Decker Lanthanide Boron Cluster, *Chem. Commun.*, 2019, **55**(54), 7864–7867, DOI: 10.1039/c9cc03807h.

53 T.-T. Chen, W.-L. Li, W.-J. Chen, X.-H. Yu, X.-R. Dong, J. Li and L.-S. Wang, Spherical Trihedral Metallo-Borospherenes, *Nat. Commun.*, 2020, **11**(1), 2766, DOI: 10.1038/s41467-020-16532-x.

54 L. S. Wang, H. S. Cheng and J. Fan, Photoelectron Spectroscopy of Size-Selected Transition Metal Clusters: Fe_n^-, n = 3-24, *J. Chem. Phys.*, 1995, **102**(24), 9480–9493, DOI: 10.1063/1.468817.

55 L. S. Wang, Photoelectron Spectroscopy of Size-Selected Boron Clusters: From Planar Structures to Borophenes

and Borospherenes, *Int. Rev. Phys. Chem.*, 2016, **35**(1), 69–142, DOI: 10.1080/0144235X.2016.1147816.

56 G. te Velde, F. M. Bickelhaupt, E. J. Baerends, C. Fonseca Guerra, S. J. A. van Gisbergen, J. G. Snijders and T. Ziegler, Chemistry with ADF, *J. Comput. Chem.*, 2001, **22**(9), 931–967, DOI: 10.1002/jcc.1056.

57 *SCM Theoretical Chemistry, ADF 2019.1*, Vrije Universiteit, Amsterdam, the Netherlands, 2019.

58 H. J. Werner, P. J. Knowles, G. Knizia, F. R. Manby and M. Schütz, Molpro: A General-Purpose Quantum Chemistry Program Package, *Wiley Interdiscip. Rev. Comput. Mol. Sci.*, 2012, **2**(2), 242–253, DOI: 10.1002/wcms.82.

59 M. J. Frisch, G. W. Trucks, H. B. Schlegel, G. E. Scuseria, M. A. Robb, J. R. Cheeseman, G. Scalmani, V. Barone, G. A. Petersson, H. Nakatsuji, X. Li, M. Caricato, A. V. Marenich, J. Bloino, B. G. Janesko, R. Gomperts, B. Mennucci, H. P. Hratchian, J. V. Ortiz, A. F. Izmaylov, J. L. Sonnenberg, D. Williams-Young, F. Ding, F. Lipparini, F. Egidi, J. Goings, B. Peng, A. Petrone, T. Henderson, D. Ranasinghe, V. G. Zakrzewski, J. Gao, N. Rega, G. Zheng, W. Liang, M. Hada, M. Ehara, K. Toyota, R. Fukuda, J. Hasegawa, M. Ishida, T. Nakajima, Y. Honda, O. Kitao, H. Nakai, T. Vreven, K. Throssell, J. A. Montgomery Jr, J. E. Peralta, F. Ogliaro, M. J. Bearpark, J. J. Heyd, E. N. Brothers, K. N. Kudin, V. N. Staroverov, T. A. Keith, R. Kobayashi, J. Normand, K. Raghavachari, A. P. Rendell, J. C. Burant, S. S. Iyengar, J. Tomasi, M. Cossi, J. M. Millam, M. Klene, C. Adamo, R. Cammi, J. W. Ochterski, R. L. Martin, K. Morokuma, O. Farkas, J. B. Foresman and D. J. Fox, *Gaussian 16, Revision C.01*, Gaussian, Inc., Wallingford CT, 2016.

60 C. Adamo and V. Barone, Toward Reliable Density Functional Methods without Adjustable Parameters: The PBE0 Model, *J. Chem. Phys.*, 1999, **110**(13), 6158–6170, DOI: 10.1063/1.478522.

61 E. Van Lenthe and E. J. Baerends, Optimized Slater-Type Basis Sets for the Elements 1-118, *J. Comput. Chem.*, 2003, **24**(9), 1142–1156, DOI: 10.1002/jcc.10255.

62 E. van Lenthe, R. van Leeuwen, E. J. Baerends and J. G. Snijders, Relativistic Regular Two-Component Hamiltonians, *Int. J. Quantum Chem.*, 1996, **57**(3), 281–293, DOI: 10.1002/(SICI)1097-461X(1996)57:3<281::AID-QUA2>3.0.CO;2-U.

63 X. Cao and M. Dolg, Valence Basis Sets for Relativistic Energy-Consistent Small-Core Lanthanide Pseudopotentials, *J. Chem. Phys.*, 2001, **115**(16), 7348–7355, DOI: 10.1063/1.1406535.

64 X. Cao and M. Dolg, Basis Set Limit Extrapolation of ACPF and CCSD(T) Results for the Third and Fourth Lanthanide Ionization Potentials, *Chem. Phys. Lett.*, 2001, **349**(5–6), 489–495, DOI: 10.1016/S0009-2614(01)01211-8.

65 T. H. Dunning, Gaussian Basis Sets for Use in Correlated Molecular Calculations. I. The Atoms Boron through Neon and Hydrogen, *J. Chem. Phys.*, 1989, **90**(2), 1007–1023, DOI: 10.1063/1.456153.

66 E. van Lenthe, J. G. Snijders and E. J. Baerends, The Zero-order Regular Approximation for Relativistic Effects: The Effect of Spin-Orbit Coupling in Closed Shell Molecules, *J. Chem. Phys.*, 1996, **105**(15), 6505–6516, DOI: 10.1063/1.472460.

67 M. Douglas and N. M. Kroll, Quantum Electrodynamical Corrections to the Fine Structure of Helium, *Ann. Phys.*, 1974, **82**(1), 89–155, DOI: 10.1016/0003-4916(74)90333-9.

68 B. A. Hess, Applicability of the No-Pair Equation with Free-Particle Projection Operators to Atomic and Molecular Structure Calculations, *Phys. Rev. A*, 1985, **32**(2), 756–763, DOI: 10.1103/PhysRevA.32.756.

69 J. D. Rolfes, F. Neese and D. A. Pantazis, All-electron Scalar Relativistic Basis Sets for the Elements Rb–Xe, *J. Comput. Chem.*, 2020, **41**(20), 1842–1849, DOI: 10.1002/jcc.26355.

70 P. R. T. Schipper, O. V. Gritsenko, S. J. A. Van Gisbergen and E. J. Baerends, Molecular Calculations of Excitation Energies and (Hyper)Polarizabilities with a Statistical Average of Orbital Model Exchange-Correlation Potentials, *J. Chem. Phys.*, 2000, **112**(3), 1344–1352, DOI: 10.1063/1.480688.

71 J. P. Perdew, K. Burke and M. Ernzerhof, Generalized Gradient Approximation Made Simple, *Phys. Rev. Lett.*, 1996, **77**(18), 3865–3868, DOI: 10.1103/PhysRevLett.77.3865.

72 L. Pauling, The Diamagnetic Anisotropy of Aromatic Molecules, *J. Chem. Phys.*, 1936, **4**(10), 673–677, DOI: 10.1063/1.1749766.

73 P. R. Schleyer, C. Maerker, A. Dransfeld, H. Jiao and N. J. R. van Eikema Hommes, Nucleus-Independent Chemical Shifts: A Simple and Efficient Aromaticity Probe, *J. Am. Chem. Soc.*, 1996, **118**(26), 6317–6318, DOI: 10.1021/ja960582d.

74 H. Fliegl, S. Taubert, O. Lehtonen and D. Sundholm, The Gauge Including Magnetically Induced Current Method, *Phys. Chem. Chem. Phys.*, 2011, **13**(46), 20500, DOI: 10.1039/c1cp21812c.

75 R. Herges and D. Geuenich, Delocalization of Electrons in Molecules, *J. Phys. Chem. A*, 2001, **105**(13), 3214–3220, DOI: 10.1021/jp0034426.

76 D. Sundholm, H. Fliegl and R. J. F. Berger, Calculations of Magnetically Induced Current Densities: Theory and Applications, *Wiley Interdiscip. Rev. Comput. Mol. Sci.*, 2016, **6**(6), 639–678, DOI: 10.1002/wcms.1270.

77 A. D. A. Becke, New Mixing of Hartree–Fock and Local Density-functional Theories, *J. Chem. Phys.*, 1993, **98**(2), 1372–1377, DOI: 10.1063/1.464304.

78 P. J. Stephens, F. J. Devlin, C. F. Chabalowski and M. J. Frisch, Ab Initio Calculation of Vibrational Absorption and Circular Dichroism Spectra Using Density Functional Force Fields, *J. Phys. Chem.*, 1994, **98**(45), 11623–11627, DOI: 10.1021/j100096a001.

79 M. Mitoraj and A. Michalak, Natural Orbitals for Chemical Valence as Descriptors of Chemical Bonding in Transition Metal Complexes, *J. Mol. Model.*, 2007, **13**(2), 347–355, DOI: 10.1007/s00894-006-0149-4.

80 J. X. Zhang, F. K. Sheong and Z. Lin, Unravelling Chemical Interactions with Principal Interacting Orbital Analysis, *Chem.–A Eur. J.*, 2018, **24**(38), 9639–9650, DOI: 10.1002/chem.201801220.

81 D. Y. Zubarev and A. I. Boldyrev, Developing Paradigms of Chemical Bonding: Adaptive Natural Density Partitioning, *Phys. Chem. Chem. Phys.*, 2008, **10**(34), 5207–5217, DOI: 10.1039/b804083d.

82 T. Lu and F. M. Chen, A Multifunctional Wavefunction Analyzer, *J. Comput. Chem.*, 2012, **33**(5), 580–592, DOI: 10.1002/jcc.22885.

83 I. Mayer, Bond Order and Valence Indices: A Personal Account, *J. Comput. Chem.*, 2007, **28**(1), 204–221, DOI: 10.1002/jcc.20494.

84 M. S. Gopinathan and K. Jug, Valency. I. A Quantum Chemical Definition and Properties, *Theor. Chim. Acta*, 1983, **63**(6), 497–509, DOI: 10.1007/BF02394809.

85 A. Michalak, R. L. Dekock and T. Ziegler, Bond Multiplicity in Transition-Metal Complexes: Applications of Two-Electron Valence Indices, *J. Phys. Chem. A*, 2008, **112**(31), 7256–7263, DOI: 10.1021/jp800139g.

86 R. F. Nalewajski, J. Mrozek and A. Michalak, Two-Electron Valence Indices from the Kohn-Sham Orbitals, *Int. J. Quantum Chem.*, 1997, **61**(3), 589–601, DOI: 10.1002/(SICI)1097-461X(1997)61:3<589::AID-QUA28>3.0.CO;2-2.

87 R. O. Jones and O. Gunnarsson, The Density Functional Formalism, Its Applications and Prospects, *Rev. Mod. Phys.*, 1989, **61**(3), 689–746, DOI: 10.1103/RevModPhys.61.689.

88 J. Li, X. Li, H.-J. Zhai and L.-S. Wang, Au_{20} : A Tetrahedral Cluster, *Science*, 2003, **299**(5608), 864–867, DOI: 10.1126/science.1079879.

89 W. L. Li, J. Su, T. Jian, G. V. Lopez, H. S. Hu, G. J. Cao, J. Li and L. S. Wang, Strong Electron Correlation in UO_2^-: A Photoelectron Spectroscopy and Relativistic Quantum Chemistry Study, *J. Chem. Phys.*, 2014, **140**(9), DOI: 10.1063/1.4867278.

90 J. Su, W. L. Li, G. V. Lopez, T. Jian, G. J. Cao, W. L. Li, W. H. E. Schwarz, L. S. Wang and J. Li, Probing the Electronic Structure and Chemical Bonding of Mono-Uranium Oxides with Different Oxidation States: UO_x^- and UO_x (x = 3-5), *J. Phys. Chem. A*, 2016, **120**(7), 1084–1096, DOI: 10.1021/acs.jpca.5b11354.

91 Z. L. Wang, H. S. Hu, L. von Szentpály, H. Stoll, S. Fritzsche, P. Pyykkö, W. H. E. Schwarz and J. Li, Understanding the Uniqueness of 2p Elements in Periodic Tables, *Chem.–A Eur. J.*, 2020, **26**(67), 15558–15564, DOI: 10.1002/chem.202003920.

92 D. R. Lonsdale and L. Goerigk, The One-Electron Self-Interaction Error in 74 Density Functional Approximations: A Case Study on Hydrogenic Mono- And Dinuclear Systems, *Phys. Chem. Chem. Phys.*, 2020, **22**(28), 15805–15830, DOI: 10.1039/d0cp01275k.

93 R. G. Pearson, The Second-Order Jahn-Teller Effect, *J. Mol. Struct.: THEOCHEM*, 1983, **103**, 25–34, DOI: 10.1016/0166-1280(83)85006-4.

94 J. C. Santos, W. Tiznado, R. Contreas and P. Fuentealba, Sigma-Pi Separation of the Electron Localization Function and Aromaticity, *J. Chem. Phys.*, 2004, **120**(4), 1670–1672, DOI: 10.1063/1.1635799.

95 Z.-J. Lv, Z. Huang, J. Shen, W.-X. Zhang and Z. Xi, Well-Defined Scandacyclopropenes: Synthesis, Structure, and Reactivity, *J. Am. Chem. Soc.*, 2019, **141**(51), 20547–20555, DOI: 10.1021/jacs.9b11631.

96 B. J. R. Cuyacot and C. Foroutan-Nejad, $[\{Th(C_8H_8)Cl_2\}_3]^{2-}$ Is Stable but Not Aromatic, *Nature*, 2022, **603**(7902), E18–E20, DOI: 10.1038/s41586-021-04319-z.

97 Z. Badri, S. Pathak, H. Fliegl, P. Rashidi-Ranjbar, R. Bast, R. Marek, C. Foroutan-Nejad and K. Ruud, All-Metal Aromaticity: Revisiting the Ring Current Model among Transition Metal Clusters, *J. Chem. Theory Comput.*, 2013, **9**(11), 4789–4796, DOI: 10.1021/ct4007184.

98 C. Foroutan-Nejad, J. Vícha and A. Ghosh, Relativity or Aromaticity? A First-Principles Perspective of Chemical Shifts in Osmabenzene and Osmapentalene Derivatives, *Phys. Chem. Chem. Phys.*, 2020, **22**(19), 10863–10869, DOI: 10.1039/D0CP01481H.

99 C. Foroutan-Nejad, Is NICS a Reliable Aromaticity Index for Transition Metal Clusters?, *Theor. Chem. Acc.*, 2015, **134**(2), 8, DOI: 10.1007/s00214-015-1617-7.

100 M. Orozco-Ic, N. D. Charistos, A. Muñoz-Castro, R. Islas, D. Sundholm and G. Merino, Core-Electron Contributions to the Molecular Magnetic Response, *Phys. Chem. Chem. Phys.*, 2022, **24**(20), 12158–12166, DOI: 10.1039/D1CP05713H.

101 C. Foroutan-Nejad, S. Shahbazian and P. Rashidi-Ranjbar, The Electron Density vs. NICS Scan: A New Approach to Assess Aromaticity in Molecules with Different Ring Sizes, *Phys. Chem. Chem. Phys.*, 2010, **12**(39), 12630, DOI: 10.1039/c004254d.

102 C. Foroutan-Nejad, Z. Badri, S. Shahbazian and P. Rashidi-Ranjbar, The Laplacian of Electron Density versus $NICS_{zz}$ Scan: Measuring Magnetic Aromaticity among Molecules with Different Atom Types, *J. Phys. Chem. A*, 2011, **115**(45), 12708–12714, DOI: 10.1021/jp203681x.

103 A. C. Castro, E. Osorio, J. O. C. Jiménez-Halla, E. Matito, W. Tiznado and G. Merino, Scalar and Spin–Orbit Relativistic Corrections to the NICS and the Induced Magnetic Field: The Case of the E_{12}^{2-} Spherenes (E = Ge, Sn, Pb), *J. Chem. Theory Comput.*, 2010, **6**(9), 2701–2705, DOI: 10.1021/ct100304c.

104 M. Orozco-Ic, J. Barroso, R. Islas and G. Merino, Delocalization in Substituted Benzene Dications: A Magnetic Point of View, *ChemistryOpen*, 2020, **9**(6), 657–661, DOI: 10.1002/open.202000105.

105 J. Vícha, M. Straka, M. L. Munzarová and R. Marek, Mechanism of Spin–Orbit Effects on the Ligand NMR Chemical Shift in Transition-Metal Complexes: Linking NMR to EPR, *J. Chem. Theory Comput.*, 2014, **10**(4), 1489–1499, DOI: 10.1021/ct400726y.

106 L. Alvarez-Thon and W. Caimanque-Aguilar, Spin-Orbit Effects on Magnetically Induced Current Densities in the

M_4^{2-} (M = B, Al, Ga, In, Tl) Clusters, *Chem. Phys. Lett.*, 2017, **671**, 118–123, DOI: 10.1016/j.cplett.2017.01.027.

107 A. E. Kuznetsov and A. I. Boldyrev, Theoretical Evidence of Aromaticity in X_3^- (X = B, Al, Ga) Species, *Struct. Chem.*, 2002, **13**(2), 141–148, DOI: 10.1023/A:1015704515336.

108 X. Chen, T. T. Chen, W. L. Li, J. B. Lu, L. J. Zhao, T. Jian, H. S. Hu, L. S. Wang and J. Li, Lanthanides with Unusually Low Oxidation States in the PrB_3^- and PrB_4^- Boride Clusters, *Inorg. Chem.*, 2019, **58**(1), 411–418, DOI: 10.1021/acs.inorgchem.8b02572.

109 M. Zhou, L. Andrews, J. Li and B. E. Bursten, Reaction of Laser-Ablated Uranium Atoms with CO: Infrared Spectra of the CUO, CUO^-, OUCCO, $(\eta^2-C_2)UO_2$, and $U(CO)_x$ (x = 1–6) Molecules in Solid Neon, *J. Am. Chem. Soc.*, 1999, **121**(41), 9712–9721, DOI: 10.1021/ja9921322.

110 J. Su, S. Hu, W. Huang, M. Zhou and J. Li, On the Oxidation States of Metal Elements in MO_3^- (M=V, Nb, Ta, Db, Pr, Gd, Pa) Anions, *Sci. China Chem.*, 2016, **59**(4), 442–451, DOI: 10.1007/s11426-015-5481-z.

111 Y. Zheng, C.-S. Cao, W. Ma, T. Chen, B. Wu, C. Yu, Z. Huang, J. Yin, H.-S. Hu, J. Li, W.-X. Zhang and Z. Xi, 2-Butene Tetraanion Bridged Dinuclear Samarium(III) Complexes via Sm(II)-Mediated Reduction of Electron-Rich Olefins, *J. Am. Chem. Soc.*, 2020, **142**(24), 10705–10714, DOI: 10.1021/jacs.0c01690.

112 Y. Xiao, X.-K. Zhao, T. Wu, J. T. Miller, H.-S. Hu, J. Li, W. Huang and P. L. Diaconescu, Distinct Electronic Structures and Bonding Interactions in Inverse-Sandwich Samarium and Ytterbium Biphenyl Complexes, *Chem. Sci.*, 2021, **12**(1), 227–238, DOI: 10.1039/D0SC03555F.